Radiation Modeling of a Hydrogen-Fueled Scramjet

Andrew J. Crow[*] and Iain D. Boyd[†]

University of Michigan, Ann Arbor, MI, 48105

Vincent E. Terrapon[‡]

Stanford University, Stanford, CA, 94305

With the difficulty and cost of full-scale flight experiments, the design of scramjet engines relies heavily on computational simulations. Radiation may play an important role in wall heating and flow cooling of scramjets. However, very few studies have focused on such. The present analysis is based on three-dimensional turbulent reacting flow simulations of the HyShot II hydrogen fueled scramjet engine running at flight conditions of Mach 7.4. A one-dimensional Discrete Ordinates Method analysis with a narrow band averaged spectral model is employed to determine wall heating and flow cooling from thermal radiation. The one-dimensional Discrete Ordinates Method is verified against a three-dimensional ray tracing method. The radiative species considered are H_2O and OH. The radiative heat flux is on the order of 10 kW/m², which is 0.1-0.2% of the total convective wall heat flux. Flow cooling due to radiation is found to be on the order of 2 K. Sensitivity analysis shows that radiation is highly dependent on chamber size, temperature, pressure and radiative species mole fraction. Variations in these factors can explain the differences between previous analyses in the literature that studied hypothetical engines and the current work that models an existing scramjet.

Nomenclature

A	Radiative Transfer Equation Linear Operator Matrix
B	Blackbody Intensity, W/(m²Hz)
F	Heat Flux, W/(m²)
I	Radiative Intensity, W/(m²Hz)
P	Pressure, Pa
Q	Radiative Transfer Equation Source Vector
S	Line Strength, 1/m
R	Residual Matrix
T	Temperature, K
U	Identity Matrix
X	Mole Fraction
a	Quadrature Weight
f	Scattering Redistribution Function
i	Location Index
j	Ordinate Index
j'	Secondary Ordinate Index
k	Frequency Index
n	Species Index
u	Scaler Cell Quantity
x	Streamwise Position, m
y	Spanwise Position, m

[*]Graduate Student, Student Member AIAA, email: ajcrow@umich.edu

[†]Professor, Fellow AIAA, email: iainboyd@umich.edu

[‡]Current address: Assistant Professor, University of Liege, email: vincent.terrapon@ulg.ac.be

American Institute of Aeronautics and Astronautics

z	Vertical Position, m
ϕ	Ordinate Angle Relative to Path, rad
ϕ'	Secondary Ordinate Angle Relative to Path, rad
κ	Extinction Coefficient, 1/m
μ	Ordinate Angle Factor Relative to Path
ν	Frequency, Hz
θ	Azimuthal Angle, rad
θ'	Secondary Azimuthal Angle, rad
τ	Optical Depth
Ψ	Adjoint Matrix
Ω	Solid Angle, sr
Subscript	
0	Reference State
I	Intensity Residual
abs	Absorption
atm	Atmospheric Pressure
max	Domain Upper Limit
min	Domain Lower Limit
sca	Scattering
ν	Frequency
Superscript	
Ω	Angular Average

I. Introduction

Unresolved questions in scramjet thermal analysis include the effects of radiative transport on the combustion chamber walls and flow-field cooling, which could significantly affect engine operation. Wall heat flux can be important for the establishment of necessary thermal protection and computational flow-field boundary conditions. In this work, the HyShot II scramjet combustor is considered, which was originally operated in a flight experiment conducted by the University of Queensland.[1] Additional ground tests have since been performed in supersonic wind tunnel experiments at the German Aerospace Center (DLR).[2] The main goal of this work is to develop a preliminary spectrally resolved model to estimate the radiative heat flux in the HyShot II Scramjet. This analysis determines the relative importance of radiative heat flux by comparing it to the convective heat flux and estimating the total flow-field temperature change due to radiative heat flux. Additionally, the sensitivities of radiative heat flux to model input parameters is analyzed.

This work presents the analysis of radiative thermal transport of the HyShot II scramjet combustor based on flow-field results calculated by the Stanford University flow-field solver (JOE).[3,4] JOE is a steady-state chemically reacting k-ω RANS solver. The radiative model presented in this paper provides the spectrally resolved radiative heat flux for different locations in the combustion chamber using a one-dimensional Discrete Ordinate Method (DOM). For the purpose of comparison, a higher fidelity spatial model is accomplished by means of a discretized three-dimensional ray tracing method. Previous works have looked at the radiative transport in a supersonic system and have found the radiative contribution to range from less than 10% to more than 90% of the total heat flux to the wall.[5–7] However, these findings are based on systems with greatly different flow-fields and geometries from those used in the HyShot II tests. Previous works show that radiative heat loss in a jet combustion chamber can lead to variations in flame properties, but these focus on flames with different chemical compositions and much slower flow speeds than those found in the HyShot II experiment.[8] The current results have a significantly lower ratio of radiative heat flux to convective flux than those in previous works. It is also shown that temperature reduction of the flow due to radiation is significantly less than predicted in previous work.[8] These differences are discussed later in this paper.

The paper is organized as follows. The Methodology section discusses the spectral and spatial methods employed for modeling radiation along with the numerical implementation scheme. The Results section discusses the CFD flow-field simulations used as inputs to the radiation analysis. It also discusses the radiative transport along several profiles taken from the flow-field. Additionally, the Results section provides data comparisons to previous works. Finally, the Conclusion section gives closing remarks and future research

American Institute of Aeronautics and Astronautics

directions.

II.   Methodology

The radiation model uses steady flow-field data as inputs, which are taken from the three-dimensional flow-field simulations computed using a chemically reacting k-ω RANS method.[3, 4, 9] A series of one-dimensional profiles are extracted from the flow-field at specific locations. The radiative thermal transport associated with these profiles is then analyzed using a one-dimensional Discrete Ordinates Method (DOM) code.[10] The code provides a first or second order spatial solution to the Radiative Transfer Equation (RTE) and employs a narrow band averaged spectral model.[11, 12] These methods allow for both spatially and spectrally resolved solutions for radiation intensity, heat flux, absorptivity, and optical depth. The DOM also solves for an entire domain which lends itself to adjoint analysis.[13, 14] Additionally, a three-dimensional discretized ray tracing method is developed to be compared to the one-dimensional DOM.[12, 15] The ray tracing method is much more spatially accurate than DOM. However, it only solves for one point at a time. Because scattering requires a nonlinear solution in the entire domain, the ray tracing method cannot directly take scattering into account.[16] The ray tracing solution is also based on the CFD flow-fields. However, the ray tracing method uses multiple flow field profiles as opposed to the single profile used by the one-dimensional DOM.

II.A.   Discrete Ordinates Method for Radiative Analysis

For the one-dimensional DOM as introduced by Chandrashekar, a plane-parallel medium is assumed for the geometry, and the radiative flux normal to the planes is calculated at all grid locations.[10] In the case of a three-dimensional geometry, a sample profile is taken of a linear trace within the medium. That profile is projected onto a plane-parallel geometry. The total spectrally resolved radiative energy flux (F_ν) along a one-dimensional flow-field profile is found by integrating the total angular intensity contributions that are normal to the plane. This is given in Eq. 1 where "μ" is the cosine of the angle "ϕ" between the ordinate and the vector normal to the plane. The coordinate system is illustrated in Fig. 1.

$$F_\nu(z) = \int_0^{2\pi} \int_0^1 I_\nu(z, \mu, \theta)\mu \, d\mu \, d\theta \tag{1}$$
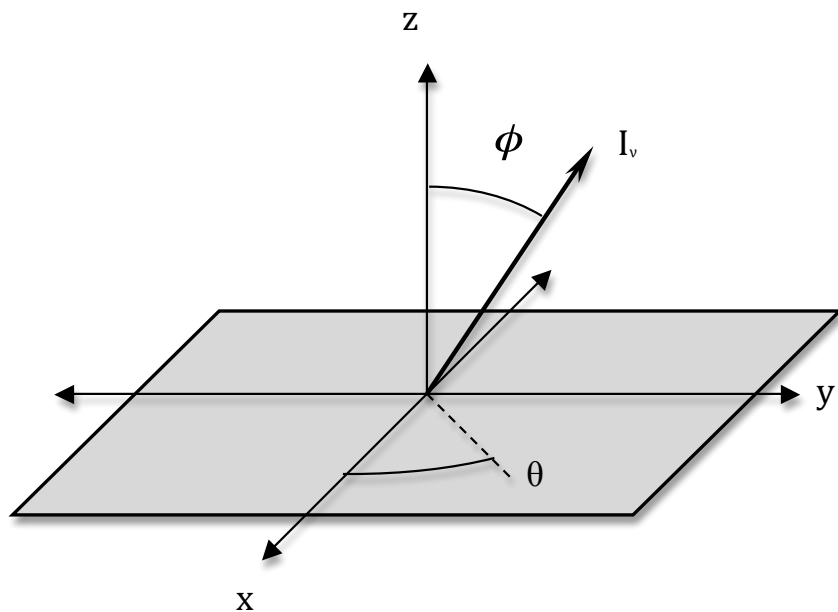

Figure 1.   Coordinate system for angular integration.

Because of the axisymmetric nature of the one-dimensional integration, the azimuthal angle can be integrated out of the equation. The angle "ϕ" is integrated by a weighted S_n quadrature as shown in Eq. 2 where "a" is a quadrature weight and "j" is a quadrature index.[17] This approach reduces the problem to solving the RTE for several discrete directions at a given frequency. The S_{12} quadrature weighting scheme described by Fiveland is used for all DOM angular integrations in this work.[17] The discrete angles are represented in Fig. 2.

$$F_\nu(z) = 2\pi \sum_j I_\nu(z,j)\mu(j)a(j) \tag{2}$$
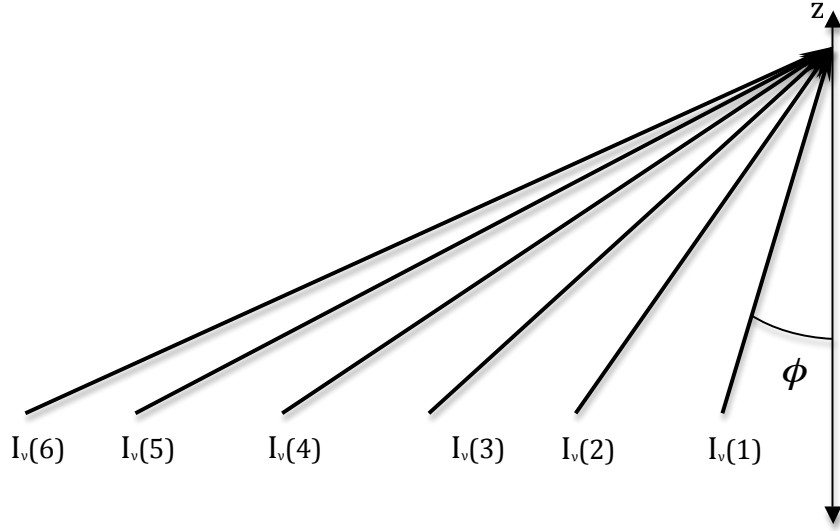

Figure 2. Discrete intensity ordinates (positive direction)

The RTE is shown in Eq. 3, where the left hand side of the equation represents the change in intensity over distance, and the terms on the right hand side represent, from left to right, extinction due to absorption, extinction due to scattering, contribution due to scattering, and contribution due to emission. The term "f" refers to the scattering redistribution function, where the angles from which the intensity is taken (the secondary angles) are denoted by primes. The term "B_ν" denotes the frequency specific blackbody intensity as determined by the Planck distribution function.[16]

$$\frac{dI_\nu(z,\mu,\phi)}{dz} = -\frac{\kappa_{abs}}{\mu}I_\nu(z,\mu,\phi) - \frac{\kappa_{sca}}{\mu}I_\nu(z,\mu,\phi) +$$
$$\frac{\kappa_{sca}}{4\pi\mu}\int_0^{2\pi}(d\phi')\int_{-1}^{1}d\mu f_\nu(z,\mu,\phi;\mu',\phi')I_\nu(z,\mu',\phi') + \frac{\kappa_{abs}}{\mu}B_\nu(T(z)) \tag{3}$$

If the system is one-dimensional with scattering, then the scattering term can be discretized using Legendre polynomials resulting in Eq. 4.[16]

$$\frac{dI_\nu(z,\mu)}{dz} = -\frac{\kappa_{abs}}{\mu}I_\nu(z,\mu) - \frac{\kappa_{sca}}{\mu}I_\nu(z,\mu) + \frac{\kappa_{sca}}{2\mu}\sum_{\mu'}a(\mu,\mu')f_\nu(\mu,\mu')I_\nu(z,\mu') + \frac{\kappa_{abs}}{\mu}B_\nu(T(z)) \tag{4}$$

This equation is spatially discretized with a first order finite difference method resulting in Eq. 5. In this case, "i," "j," "j'" and, "Δz" represent the spatial index, angular index, secondary angular index, and grid spacing, respectively. The first-order method is chosen over a second-order method because the CFD results

American Institute of Aeronautics and Astronautics

from JOE use a nonuniform grid that is incompatible with second order finite differencing methods.[18] The reduction to first order requires a finer grid spacing in order to achieve the same accuracy.

$$\frac{I_\nu(i,j) - I_\nu(i-1,j)}{\Delta z(i)} = -\frac{\kappa_{abs}(i)}{\mu(j)}I_\nu(i,j) - \frac{\kappa_{sca}(i)}{\mu(j)}I_\nu(i,j) +$$
$$\frac{\kappa_{sca}(i)}{2\mu(j)}\sum_{j'} a(j,j')f_\nu(\mu,\mu')I_\nu(i,j') + \frac{\kappa_{abs}(i)}{\mu(j)}B_\nu(T(i)) \tag{5}$$

The boundary conditions at the walls are modeled as blackbodies and represented by Eq. 6.

$$I_\nu(i,j) = B_\nu(T(i)) \tag{6}$$

When written in matrix notation, the total set of equations has the form of Eq. 7 where the matrix "A" represents the scattering, absorption and pass-through terms, and the vector "Q" represents the emission source terms. Equation 7 is solved implicitly for intensity using a Gauss-Seidel Method.[19]

$$0 = A_\nu I_\nu + Q_\nu \tag{7}$$

One important note is that if the scattering terms are not included ($\kappa_{sca} = 0$), then Eq. 7 can be solved in one iteration because there is no mechanism for radiation to influence itself upstream. In the case of the HyShot II combustion experiment scattering can be ignored because the high temperatures prevent fuel or water droplet formation, which means that Mie scattering is not possible. Additionally, the wavelengths considered are in the infrared regime which is not significantly affected by Rayleigh scattering.[16] Since the scattering is not significant in this case, it will be ignored in all analysis even though the DOM and the subsequent DOM sensitivity analyses are robust enough to incorporate it.[16]

II.B. Ray Tracing Method for Radiative Analysis

For the purpose of verification, a spatially discretized three-dimensional ray tracing method with a narrow band averaged spectral method is employed.[15] While the selection of paths for the ray tracing method is often chosen with a Monte Carlo scheme, a pre-determined ray spacing is opted for in this application.[12] The ray tracing method divides the entire domain into a grid of discrete rays emanating from a vertex. These rays are then traced until they encounter an obstruction. The entire path of each ray is integrated to determine the incident intensity at the vertex. The individual intensities are then angularly integrated as given in Eq. 8.

$$F_\nu = \int_0^{2\pi} \int_0^\pi I_\nu(\theta,\phi)\sin(\phi)\cos(\phi)d\phi d\theta \tag{8}$$

A numerical integration method is given by Eq. 9.[15] A diagram of an individual ray and associated solid angle is given in Fig. 3.

$$F_\nu = \sum_j I_\nu(\theta(j),\phi(j))\sin(\phi(j))\cos(\phi(j))\sin(\Delta\phi(j))\Delta\theta(j) \tag{9}$$

Because the ray tracing method cannot incorporate scattering, the governing radiative transfer equation (RTE) does not include these terms as given by Eq. 10.[12] As discussed earlier in this work, the scattering does not play a significant role in the radiative transfer in the HyShot II combustion chamber. Therefore, this is an acceptable omission.

$$\frac{I_\nu(i,j) - I_\nu(i-1,j)}{\Delta z(i)} = -\frac{\kappa_{abs}(i)}{\mu(j)}I_\nu(i,j) + \frac{\kappa_{abs}(i)}{\mu(j)}B_\nu(T(i)) \tag{10}$$

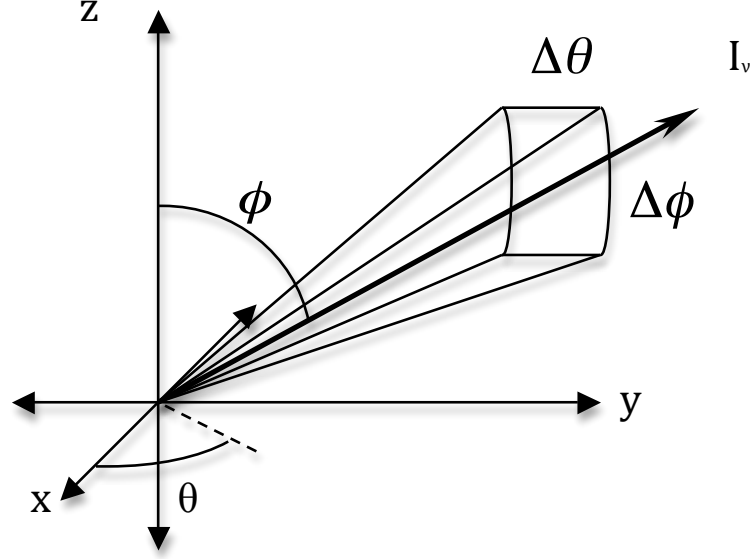American Institute of Aeronautics and Astronautics

Figure 3. Individual intensity ray with associated angular width

II.C. Spectral Model

The absorption coefficients for both the ray tracing method and the DOM are determined by a narrow band averaged spectral model.[12] Because the narrow band averaged model only uses the mean absorptivity, the Doppler and pressure broadening can be ignored.[16] From the tables given in the general appendix of the NASA Infrared Radiation Handbook, the average band strength can be calculated from Eq. 11.[20] In Eq. 11, the "P_{atm}," "$X_n(i)$," and "$T(i)$" terms are the cell pressure (in atm), radiative species mole fraction, and cell temperature (in Kelvin), respectively. "T_0" is a reference temperature determined by the spectral reference tables. The index "n" is for each radiative species. The spectral line strength "S_ν" is dependent on temperature and wavenumber and is given by the general appendix of the NASA radiation handbook.[20]

$$\kappa_{abs} = \sum_n S_\nu(T(i),n)P_{atm}(i)X(i,n)T_0/T(i) \tag{11}$$

Because a band averaged model is used, frequency specific quantities are found using averaged line strengths, which result in averaged absorption coefficients. This transforms Eqs. 11, 5, and 8 into Eqs. 12, 13, and 14, respectively.

$$\bar{\kappa}_{abs} = \sum_n \bar{S}_\nu(T(i),n)P_{atm}(i)X(i,n)T_0/T(i) \tag{12}$$

$$\frac{\bar{I}_\nu(i,j) - \bar{I}_\nu(i-1,j)}{\Delta z(i)} = -\frac{\bar{\kappa}_{abs}(i)}{\mu(j)}\bar{I}_\nu(i,j) - \frac{\bar{\kappa}_{sca}(i)}{\mu(j)}\bar{I}_\nu(i,j) + \frac{\bar{\kappa}_{sca}(i)}{2\mu(j)}\sum_l a(j,l)\bar{I}_\nu(i,l) + \frac{\bar{\kappa}_{abs}(i)}{\mu(j)}\bar{B}_\nu(T(i)) \tag{13}$$

$$\frac{\bar{I}_\nu(i,j) - \bar{I}_\nu(i-1,j)}{\Delta z(i)} = -\frac{\bar{\kappa}_{abs}(i)}{\mu(j)}\bar{I}_\nu(i,j) + \frac{\bar{\kappa}_{abs}(i)}{\mu(j)}\bar{B}_\nu(T(i)) \tag{14}$$

The spectrally resolved optical depth is calculated by integrating the spectrally resolved absorption coefficient over the traversed path as given in Eq. 15.

$$\bar{\tau}_\nu = \int_{min}^{max} \bar{\kappa}_{abs}(z)dz \tag{15}$$

This expression is then angularly averaged to obtain an estimate of optical depth as in Eq. 16.

American Institute of Aeronautics and Astronautics

$$\bar{\tau}_\nu^\Omega = \frac{\int^\Omega \bar{\tau}_\nu d\Omega}{\int^\Omega d\Omega} \tag{16}$$

The angular averaging depends on the solution scheme. For the one-dimensional DOM, the path is discretized based on the cell quantities and numerically integrated using the quadrature scheme in Eq. 17.

$$\bar{\tau}_\nu^\Omega = \sum_j a(j)/\mu(j) \sum_i \bar{\kappa}_{abs} \Delta z(i) \tag{17}$$

For the three-dimensional ray tracing method, the path is discretized along each ray, which are then averaged using a weighted area scheme in Eq. 18, where $\Delta\Omega$ is the discretized solid angle given by Eq. 19 which is derived from Eq. 9.

$$\bar{\tau}_\nu^\Omega = \frac{\sum_j \Delta\Omega(j)/\mu(j) \sum_i \bar{\kappa}_{abs}(i,j)\Delta z(i)}{\sum_j \Delta\Omega(j)/\mu(j)} \tag{18}$$

$$\Delta\Omega = \sum_j (\theta(j), \phi(j)) \sin(\phi(j)) \cos(\phi(j)) \sin(\Delta\phi(j)) \Delta\theta(j) \tag{19}$$

The total flux is calculated by a frequency integration of the spectrally resolved flux as seen in Eq. 20.

$$F(z) = \int_{\nu_{min}}^{\nu_{max}} F_\nu(z) d\nu \tag{20}$$

Because all bands are assumed independent, the total integration can be accomplished by the sum of the spectrally resolved flux multiplied by the bandwidth for each frequency as in Eq. 21.

$$F(z) = \sum_k F_\nu(z) \Delta\nu(k) \tag{21}$$

II.D. Adjoint Sensitivity

In order to determine the most pertinent factors affecting the overall wall radiative heat flux, an adjoint sensitivity method is employed for the one-dimensional DOM. The adjoint method allows for the local derivatives of a computed quantity to be calculated simultaneously with respect to numerous inputs. In this case, sensitivity of the wall radiative heat flux is calculated with respect to temperature, pressure and mole fraction within each cell. In Eq. 22, the transpose of the adjoint matrix solution $(-\Psi^T)$ relates the sensitivities of the radiative wall heat fluxes to the residuals of the cell radiative intensities. The chain rule allows for the adjoint solution to be multiplied by the derivative of the cell intensity residuals (R_I) with respect to the cell quantities (u) to multiply the adjoint solution in Eq. 22, which results in the sensitivity calculation to be split into two parts.

$$\left[\frac{\delta F(z)}{\delta u}\right] = -\Psi^T \left[\frac{\delta R_I}{\delta u}\right] \tag{22}$$

The adjoint matrix is calculated iteratively using Eq. 23. A good description of the discrete adjoint sensitivity method and means of calculating the adjoint matrix is given by Fidkowski and Darmofal.[21]

$$A_\nu^T \Psi + \left[\frac{\delta F(z)}{\delta I_\nu}\right]^T = 0 \tag{23}$$

The matrix of derivative of flux with respect to intensity for a specific location $\left[\frac{\delta F(z)}{\delta I_\nu}\right]$ is calculated in Eq. 24, which produces two derivatives $\frac{\delta F(z)}{\delta F(z)_\nu}$ and $\frac{\delta F(z)_\nu}{\delta I_\nu}$ that can be directly calculated by taking the derivative of Eqs. 21 and 2, respectively.

$$\frac{\delta F(z)}{\delta I_\nu} = \frac{\delta F(z)}{\delta F(z)_\nu} \frac{\delta F(z)_\nu}{\delta I_\nu} \tag{24}$$

The residual matrix is calculated with Eq. 25, which is the general matrix solution of Eq. 6 with the residuals explicitly added.

$$R_I = A_\nu I_\nu + Q_\nu \qquad (25)$$

The derivative of Eq. 25 with respect to the cell quantities is found in Eq. 26 with the individual terms of the A and Q matrices being readily differentiable by the cell quantities. Equation 26 closes Eq. 22.

$$\frac{\delta R_I(k)}{\delta u} = \frac{\delta A_\nu}{\delta u} I_\nu + \frac{\delta Q_\nu}{\delta u} \qquad (26)$$

The advantage of performing the sensitivity analysis this way is that the location and magnitude of flow-field sensitivities can be be calculated for the price of one additional matrix solution. This allows simulations to focus on probing the most pertinent locations and quantities.

III. Results

This section describes the test case considered and the CFD simulations of the test case. This section also describes the one-dimensional DOM radiative analysis of the test cases and discusses the comparisons of three-dimensional radiative solutions. The sensitivity analysis determines dominant quantities for use in comparing radiative flows. Finally, the section offers some comparative analysis between this work and results found in the literature.

III.A. CFD Results

The CFD results are based on the geometry of the HyShot II scramjet as described in the work of Paull et al.[1,22] The Hyshot II combustion experiment was a high atmosphere hypersonic combustion test, which was intended to gather data on scramjets, but it was not intended to provide a net-positive thrust. The experiment consisted of attaching a test combustion chamber to a rocket. The chamber is 75 mm wide and 9.8 mm high with a stream-wise length of 0.400 m. The vehicle tip (not shown) is located at x=-0.408 m. The combustion chamber entrance is located at x=-0.058 m, and the fuel is injected at x=0.000 m. The free-stream condition corresponds to those in the ground experiments performed by Karl *et al* with a pressure of 1813 Pa, a temperature of 242 K, a density of 0.0260 kg/m^3, a velocity of 2313 m/s, and a Mach number of 7.4.[2] A diagram of the flow domain with temperature profiles is given in Fig. 4, where "x," "y," and "z" represent the stream-wise, horizontal span-wise and vertical axes, respectively. In this case x=0 m, y=0 m, and z=0 m are at the injection port, the bottom wall, and the centerline respectively, as seen in Fig. 4. Because of planes of symmetry, only one-eighth of the span-wise direction is simulated and subsequently shown. The boundary conditions for the simulation are 300 K for the top and bottom of the chamber with symmetry planes for the sidewalls. The simulation employs a time averaged k-ω RANS simulation with a combustion chemistry model run on a domain size on the order of 10^7 elements.[3]

Figure 5 depicts the temperature contours for the planes from which the profiles are taken. Figure 5(a) depicts the plane that is normal to the y-axis at y=0.006 m. Figure 5(b) depicts the plane that is normal to the y-axis at y=0.00 m, which lies on the centerline. The temperatures at the centerline are significantly lower than those at y=0.006 m. The temperature is lower because the centerline lies midway between the injection ports, which are evenly spaced 0.01875m apart. The combustion products reach y=0.006 m quickly, but they do not reach the centerline until the expansion nozzle. Figure 5(c) depicts the plane normal to the main stream-wise axis at x=0.042 m. The cool fuel stream is still present, because much of the fuel is left unburnt at this point. Figure 5(d) depicts the plane normal to the main stream-wise axis at x=0.242 m. The product stream is hotter than at x=0.042m because the fuel has gone through most of its combustion. However, the products, have not reached the centerline. In Figs. 5(a) and (b), the flow moves from left to right. In Figs. 5(c) and (d), the contour plot only covers 9.375 mm of the channel width just as in Fig. 4.

Figure 6 depicts a profile of the most important flow quantities for radiative analysis at the combustion chamber exit (expansion nozzle entrance). The profile is taken perpendicular to the top and bottom walls of the combustion chamber (the "z" axis) at y=0.006 m and x=0.242m.

Several vertical profiles are extracted from the flow-field. The averaged quantities of these profiles are given in Table 1 for y =0.000 m and y=0.006 m. The centerline is chosen because it coincides with the location of the experimental temperature measurements.[2] The location of y=0.006 m is chosen because it
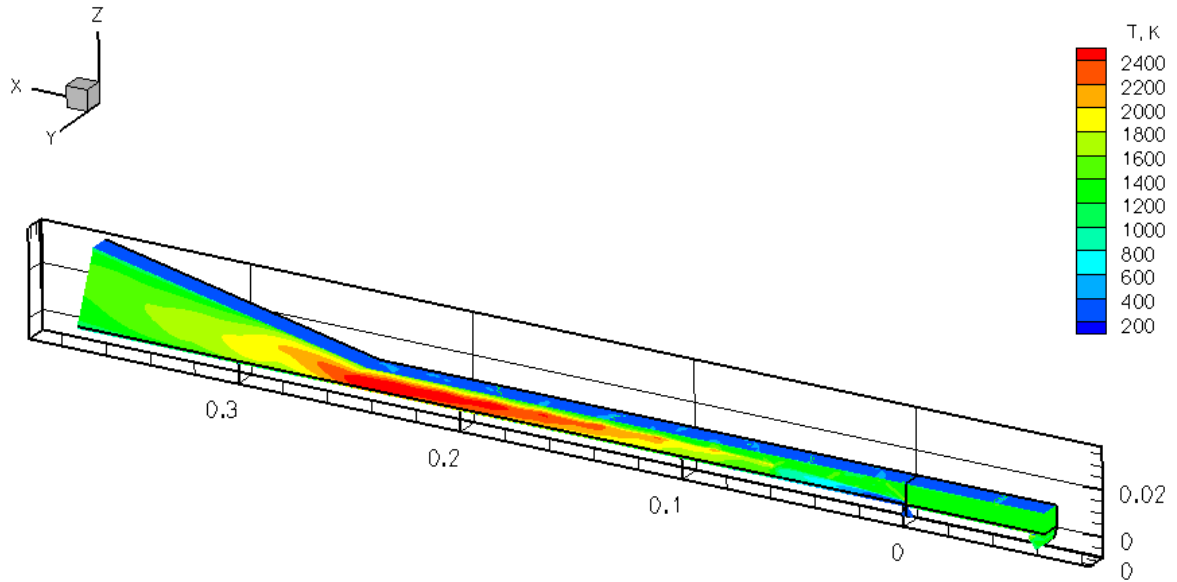
Figure 4. Computed temperature contours (K) of the flow domain. The axes "x," "y," and "z" represent the stream-wise, horizontal span-wise and vertical axes, respectively. The x=0.0 m, y=0.0 m, and z=0.0 m planes are located as shown by the black lines on the contour plot.

includes an optically thicker portion of the flame than the centerline. The stream-wise locations are chosen to be directly downstream of the injection nozzle in the combustion chamber (x=0.042 m and x=0.092 m) where the combustion is incomplete, at the combustion chamber exit (x=0.242 m) where the temperature is highest, and in the nozzle (x=0.292 m and x=0.342 m) where the flow is most homogenous. The quantities given in Table 1 are the profile averaged values, which are only provided to give a general understanding of the profile used. The quantities used as inputs to the radiative methods are spatially resolved.

III.B.   Convective Heat Flux

A main goal of this work is to compare the radiative heat fluxes to the convective heat transfer of the system. Figure 7 displays the convective heat flux to the upper and lower walls of the combustion chamber. The data-points in Fig. 7 depict the convective heat fluxes measured in the experiment by Karl *et al*,[2] and the lines are the convective heat fluxes predicted by the JOE CFD simulations.[3] Figure 7(a) depicts the CFD wall heat transfer prediction and experimental measurements at the centerline of the combustion chamber. The results given in Fig. 7(b) are the CFD wall heat fluxes at y=0.006 m and y=0.000 m. The CFD results show a large variation based on location in both the stream-wise and span-wise directions. The heat flux at the lower wall at y=0.006 m is significantly higher because the injection ports are only on the lower wall. The flame and combustion products do not reach the upper wall or centerline until the end of the combustion chamber. The heat flux increases at the lower wall at y=0.006 m as the flow moves downstream and hot combustion products increase. The heat flux decreases in the combustion chamber as the hot products spread-out. This spreading of hot combustion products causes the heat transfer to lessen at the lower wall for y=0.006 m and the heat transfer to increase at other locations. The spatially oscillatory variations in heat transfer are due to a reflecting shock-expansion interaction. As the flow passes through the nozzle starting at x=0.242 m it expands and cools which lowers the total heat flux.
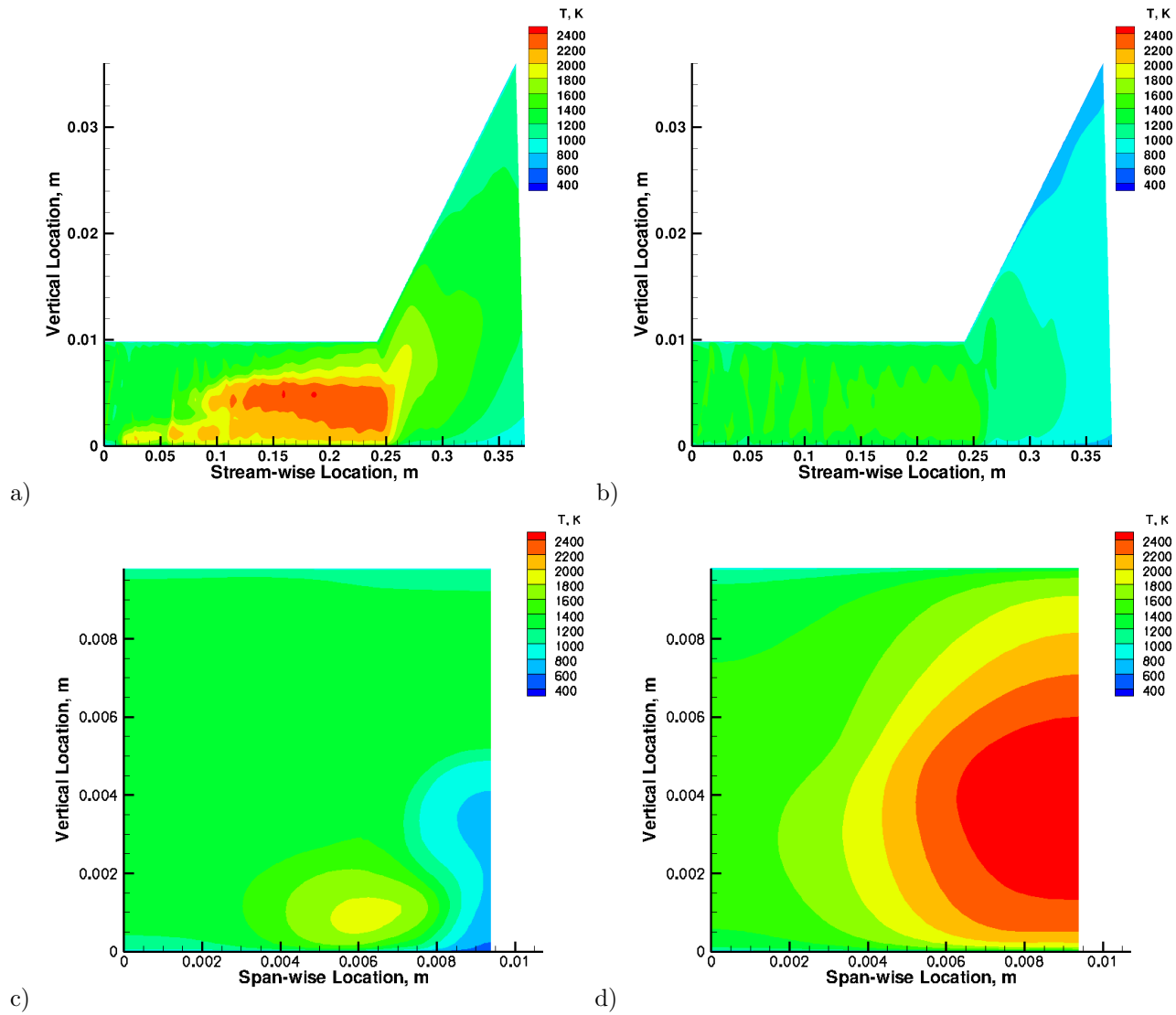
American Institute of Aeronautics and Astronautics

Figure 5. Temperature contours (K) at (a) y=0.006 m, (b) y=0.000 m (centerline), (c) x=0.042 m, and (d) x=0.242 m
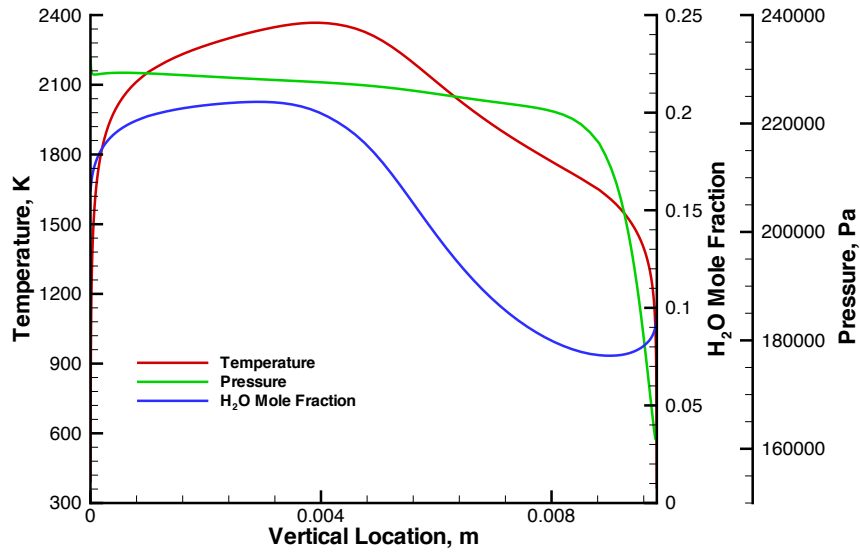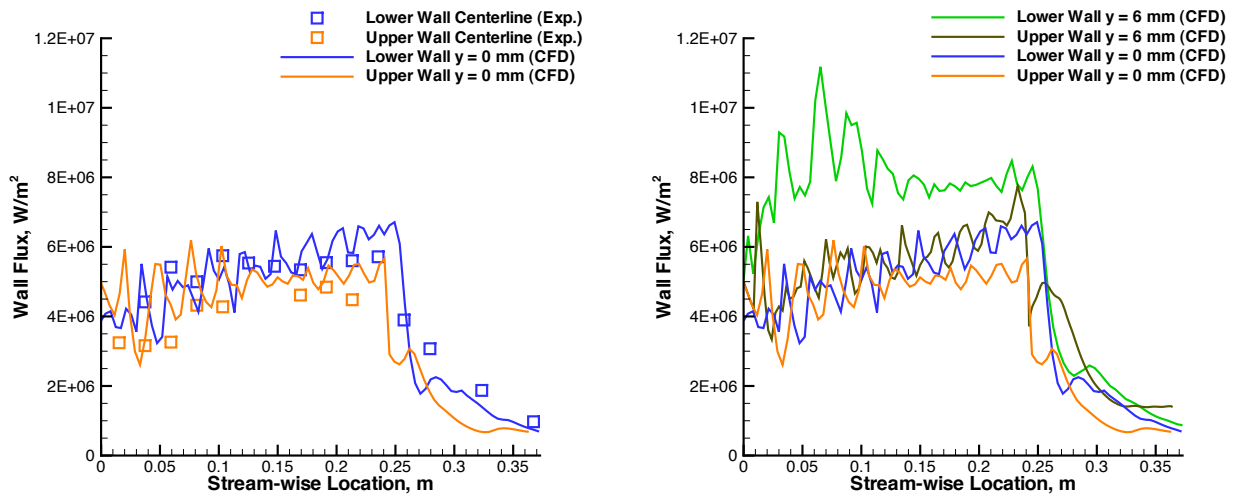
Figure 6. Flow-field profiles in the vertical direction at x=0.242m and y=0.006m

a)

b)

Figure 7. Heat flux along the steam-wise axis for top and bottom walls of the combustor at (a) experimental measurements with CFD predictions at y=0.000 m (centerline) and (b) CFD predictions at y=0.006 m and y=0.000 m

American Institute of Aeronautics and Astronautics

Table 1. Averaged quantities for profiles taken at (a) y=0.006 m and (b) y=0.000 m

Location (m)	Temperature (K)	Pressure (Pa)	Mole Fraction H_2O	Mole Fraction OH	Mole Fraction N_2	Mole Fraction O_2	Mole Fraction H_2
0.042	1140	1.41×10^5	8.14×10^{-2}	5.98×10^{-3}	0.708	0.143	4.29×10^{-2}
0.092	1250	1.79×10^5	9.97×10^{-2}	9.97×10^{-3}	0.710	0.132	3.17×10^{-2}
0.242	1440	2.08×10^5	0.137	1.13×10^{-2}	0.721	0.115	8.01×10^{-3}
0.292	1000	6.12×10^4	0.122	1.08×10^{-2}	0.730	0.125	4.24×10^{-3}
0.342	843	3.15×10^4	0.121	1.17×10^{-2}	0.728	0.124	4.53×10^{-3}

a) y=0.006 m

Location (m)	Temperature (K)	Pressure (Pa)	Mole Fraction H_2O	Mole Fraction OH	Mole Fraction N_2	Mole Fraction O_2	Mole Fraction H_2
0.042	1220	1.02×10^5	0.00	0.00	7.90×10^{-1}	2.10×10^{-1}	0.00
0.092	1220	1.02×10^5	0.00	0.00	7.90×10^{-1}	2.10×10^{-1}	0.00
0.242	770	1.05×10^5	0.00	0.00	7.90×10^{-1}	2.10×10^{-1}	0.00
0.292	770	1.05×10^5	3.23×10^{-4}	1.21×10^{-5}	7.90×10^{-1}	2.10×10^{-1}	1.21×10^{-6}
0.342	624	1.04×10^5	6.14×10^{-4}	1.08×10^{-5}	7.90×10^{-1}	2.10×10^{-1}	3.82×10^{-6}

b) y=0.000 m

III.C. Spectrally Resolved Radiative Heat Fluxes

A series of profiles are analyzed along the axis normal to the upper and lower walls. All of the profiles are processed by the one-dimensional DOM code using the S_{12} quadrature scheme.[17] The walls are assumed to be black, nonreflective, and nonradiative. These boundary conditions are chosen because only the net flow radiation is of interest. The spectral characteristics for the incident flux to the lower wall for the combustion chamber are displayed in Fig. 8. The figure has the spectrally resolved wall flux and the spectrally resolved optical depth. The profiles are taken at the plane y=0.006 m at locations directly downstream of the fuel injector (x=0.042 m and x=0.092 m), at the combustion expansion nozzle entrance (x=0.242 m), and in the nozzle (x=0.292 m and x=0.342 m). The combustion chamber exit is the most radiatively intense and optically thick profile, because the combustion products are most prevalent and the flame structure is intact. The peak optical depth is smaller than 1. Additionally, the spectrally resolved heat flux still shows many spectral characteristics indicating that it differs greatly from a blackbody curve.

The one-dimensional DOM is compared to the three-dimensional discretized ray tracing method. With a spatial resolution of 5 degrees, the ray tracing method employs 1296 rays. A convergence study shows that refining the angular spacing by halving the grid spacing results in a change of less than 0.1%. The results of the spectrally resolved three-dimensional case are displayed in Fig. 9. Figure 9(a) shows the spectrally resolved heat flux, which is approximately a factor of two smaller than the one-dimensional calculations. The optical depth is shown in Fig. 9(b), which shows a lower optical depth than that of the one-dimensional case. While less accurate than the three-dimensional ray tracing method, the one-dimensional DOM for combustion chambers may still serve the purpose of providing rapid analysis. The advantage of DOM is that only one profile is extracted and processed as opposed to over a thousand profiles with the ray tracing method. This allows DOM to function on the order of 10 seconds while ray tracing runs on the order of 1000-3000 seconds.

A summary of heat fluxes for the optically thicker case (y = 0.006 m) are given in Table 2. The peak radiative heat flux in these cases is less than one percent of the convective heat flux to the walls. Because the flow-field is still optically thin, there are only slight differences between the radiative fluxes to the upper and lower walls. At x=0.042 m, the radiation is very small due to the low concentration of radiative species due to only partial combustion. At x=0.092 m, the radiation increases slightly. At x=0.242 m, the radiation peaks due to high flame temperature and concentration of combustion products. The profile at x=0.292 m yields a decrease in radiation because the flow expands and cools in the nozzle. The profile at x=0.342 m is even cooler than the profile at x=0.292 m. The general trend for the radiative heat flux is to rise to a peak at the combustion chamber exit then lessen throughout the nozzle. The general trend for optical depth is for the depth to increase in the combustion chamber. The optical depth reaches its maximum in the nozzle and steadily decreases until the exit. The rising optical depth in the combustion chamber is explained by the introduction of radiative species through the combustion process. The peak at the nozzle entrance occurs because the maximum concentration of radiative species exist there. Also, the flame structure is still intact,

American Institute of Aeronautics and Astronautics
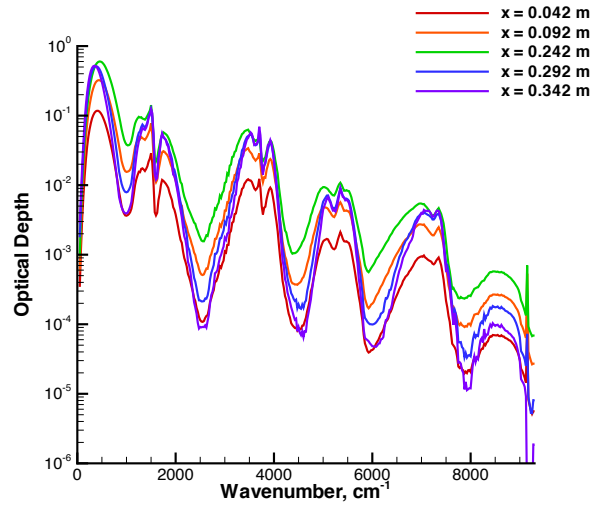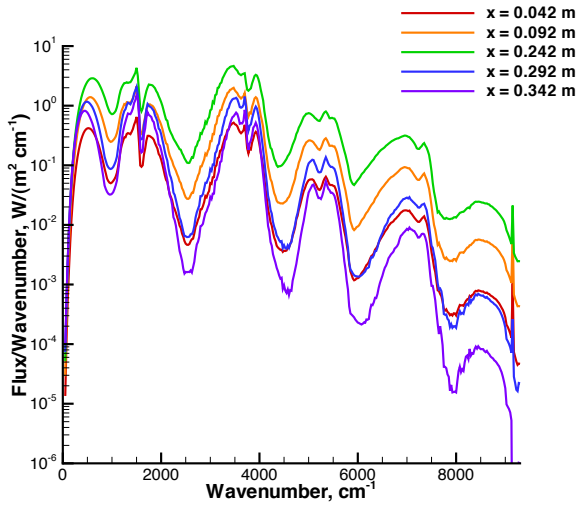
Figure 8. Radiative solutions for one-dimensional DOM (a) spectrally resolved heat flux and (b) spectrally resolved optical depth vs. wavenumber at x=0.242 m and y=0.006 m
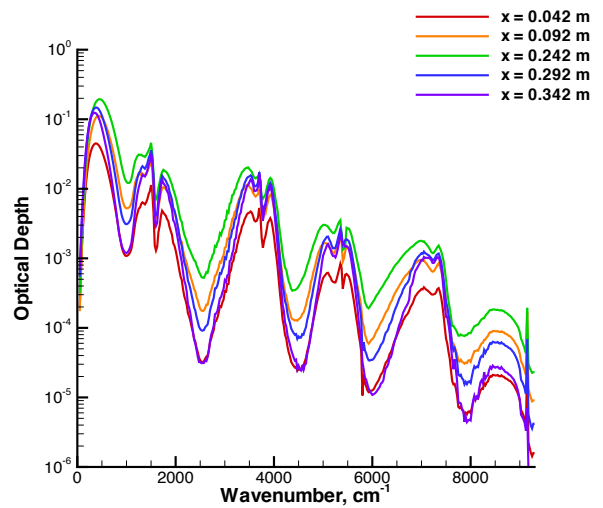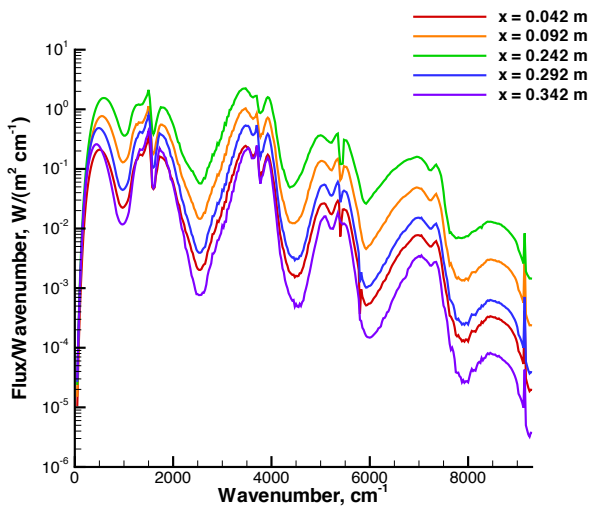
Figure 9. Radiative solutions for three-dimensional ray tracing method (a) spectrally resolved heat flux and (b) spectrally resolved optical depth vs. wavenumber at x=0.242 m and y=0.006 m

American Institute of Aeronautics and Astronautics

which means that the profile passes through a disproportionately high concentration of radiative species. This results in a high optical depth through the profile. The lowering of optical depth in the nozzle is explained by the lowering of radiative species concentrations there. Although the same amount of radiative species exist at the combustion chamber exit as do in the nozzle, the species are much more homogeneously distributed. As such, the optical depth of any profile will not be as high as the peak profile found at the combustion chamber exit.

In order to probe the validity of the one-dimensional DOM analysis other profiles are taken along the centerline (y=0.000 m). Table 3(a) compares the radiative DOM results with the convective CFD results. The DOM results at the centerline do not have any radiative flux within the combustion chamber and very little in the nozzle. This is because the radiative combustion products do not reach the centerline between the injection ports until the nozzle. Even there, they only arrive in trace amounts. The DOM only takes one profile trace into account. Therefore, if the path does not have radiative species, then the radiative flux will not exist in a calculable amount. The ray tracing results are given in Table 3(b). Because it takes the full three-dimensional domain into account, as opposed to a single one-dimensional profile, the ray tracing method can still garner heat fluxes in non radiative areas similar to those of the most radiative areas. The ray tracing method employs many paths which pass through the entire domain. As such, it will calculate radiative heat flux from the flame structure even though it is not adjacent to the measurement point. Because of the large variation in the temperature and heat flux, the DOM results differ by several orders of magnitude from the centerline to the most radiative portions. Therefore, DOM traces must be carefully chosen to obtain a good representative estimation of the radiative fluxes. The case of x=0.006 m appears to be a reasonable estimate.

Table 2. Comparison of convective and radiative heat fluxes using the (a) one-dimensional DOM and (b) three-dimensional ray tracing method at y=0.006 m

Location	Radiative Flux Upper Wall	Radiative Flux Lower Wall	Convective Flux Upper Wall	Convective Flux Lower Wall	Flux Percentage Upper Wall	Flux Percentage Lower Wall
(m)	(W/m^2)	(W/m^2)	(W/m^2)	(W/m^2)	(%)	(%)
0.042	813	812	4.31×10^6	3.94×10^6	1.89×10^{-2}	2.06×10^{-2}
0.092	3120	3120	4.21×10^6	5.80×10^6	7.39×10^{-2}	5.37×10^{-2}
0.242	7740	7770	5.16×10^6	6.38×10^6	0.150	0.122
0.292	2130	2130	2.63×10^6	2.05×10^6	8.09×10^{-2}	0.104
0.342	1230	1230	1.44×10^6	2.61×10^6	8.54×10^{-2}	4.72×10^{-2}

a) one-dimensional DOM

Location	Radiative Flux Lower Wall	Convective Flux Lower Wall	Flux Percentage Lower Wall
(m)	(W/m^2)	(W/m^2)	(%)
0.042	467	3.94×10^6	1.18×10^{-2}
0.092	2150	5.80×10^6	3.70×10^{-2}
0.242	5360	6.38×10^6	8.40×10^{-2}
0.292	1560	2.05×10^6	7.59×10^{-2}
0.342	734	2.61×10^6	2.81×10^{-2}

b) three-dimensional ray tracing

III.D. Sensitivity Analysis

Another area of interest is to determine which cell quantities have the greatest effect on the radiative heat flux. This serves to give a basis for comparing different flows. To do so, the one-dimensional DOM solutions are processed using an adjoint sensitivity analysis. Figure 10 demonstrates the sensitivity of the wall radiative heat fluxes to different cell quantities. In order to provide an even basis for comparison among the sensitivities, the cell sensitivity is divided by the ratio of the wall flux to the cell quantity $\left(\frac{\delta F}{\delta u}(z)/\frac{F}{u(z)}\right)$. This indicates the relative amount each quantity contributes to the overall radiative heat flux. Temperature is found to be the most important quantity, which is followed by pressure and water vapor mole fraction. The hydroxyl radical mole fraction has a minor impact on radiative heat flux. All other quantities have negligible impact in this model. Figure 10(a) demonstrates the sensitivity at x=0.042 m. The sensitivities are highest at x = 0.042 m because the radiating part of the flow is concentrated into a small number of cells as the flame has not spread to the entire fuel stream. Figure 10(b) demonstrates the sensitivity at x=0.092

Table 3. Comparison of convective and radiative heat fluxes using the (a) one-dimensional DOM and (b) three-dimensional ray tracing method at y=0.000 m

Location	Radiative Flux Upper Wall	Radiative Flux Lower Wall	Convective Flux Upper Wall	Convective Flux Lower Wall	Flux Percentage Upper Wall	Flux Percentage Lower Wall
(m)	(W/m^2)	(W/m^2)	(W/m^2)	(W/m^2)	(%)	(%)
0.042	0.00	0.00	8.30×10^6	4.05×10^6	0.00	0.00
0.092	0.00	0.00	8.20×10^6	4.23×10^6	0.00	0.00
0.242	0.00	0.00	8.08×10^6	4.77×10^6	0.00	0.00
0.292	0.977	0.977	2.54×10^6	2.42×10^6	3.84×10^{-5}	4.04×10^{-5}
0.342	2.10	2.10	1.39×10^6	1.28×10^6	1.51×10^{-4}	1.64×10^{-4}

a) one-dimensional DOM

Location	Radiative Flux Lower Wall	Convective Flux Lower Wall	Flux Percentage Lower Wall
(m)	(W/m^2)	(W/m^2)	(%)
0.042	391	4.05×10^6	9.66×10^{-3}
0.092	919	4.23×10^6	2.17×10^{-2}
0.242	2870	4.77×10^6	6.02×10^{-2}
0.292	1240	2.42×10^6	5.13×10^{-2}
0.342	1200	1.28×10^6	9.35×10^{-2}

b) three-dimensional ray tracing

m. The bimodal sensitivity comes from the flame structure wrapping around the cool fuel stream. Figures 10(c) and (d) demonstrate the sensitivity at x=0.242 m for the lower and upper walls respectively. The flame here is larger and spread-out. Thus, the sensitivity is much more evenly distributed. Also, the two profiles are almost identical due to the low optical depth. The analysis supports the expectation that temperature, pressure and H_2O mole fraction are the most important quantities in determination of radiative heat flux, which can be used in comparing different flows.

III.E.   Comparisons to Other Works

The current simulations show a significantly smaller radiative heat flux and optical depth than those obtained in similar previous works. In this case the simulation of the physical combustion experiment is compared to simulations of hypothetical combustion engines. The radiative heat flux to the wall was predicted by Nelson to be on the order of 10% of the convective heat flux for a hydrogen-fueled scramjet engine.[5] A series of test cases are run using DOM that compare the radiative heat flux from the input data for Nelson's combustion conditions with the radiative heat flux from the JOE CFD solution. Because of the different geometries used in the paper by Nelson and the HyShot II, a standard geometry is needed to compare the sizes of the problem. The geometry chosen is a plane-parallel configuration. This reduces the comparisons to only the medium and one spatial dimension. It also makes the one-dimensional DOM the most applicable method for analyzing the test cases.[16] The baseline case is taken as the solution at y= 0.006 m at the entrance of the HyShot II expansion nozzle (x=0.242 m). The boundary conditions are two parallel cold nonreflective plates spaced 0.0098 m apart. The HyShot II CFD solution is then linearly scaled to fit into the geometry used by Nelson and simulated again using the DOM. The four flow conditions mentioned in Nelson's paper are also used. The boundary conditions for these cases are also two parallel cold nonreflective plates spaced 0.0665 m apart. The radiative solution to Nelson's flow conditions are then repeated on the geometry for the HyShot II combustor. This means that all flow solutions are simulated using both geometries with the one-dimensional DOM code. Table 4 gives the results of these simulations. Dependence on combustor size is apparent in Table 4 where changes in geometry result in changes in wall heat flux from a factor of 5 to 7. The flow conditions considered by Nelson are uniform and generally hotter, higher pressure, and more concentrated with H_2O than the CFD results from JOE. The exception is the Mach7.67(b) example, which is a cooler flow with lower H_2O concentration than the HyShot II simulation. All of the cases taken from Nelson are more radiative than the corresponding JOE simulations, with the exception of the Mach7.67(b) case. This supports the results of the sensitivity analysis which states that temperature, pressure and concentration of H_2O are the factors which increase the radiative heat flux. Additionally, the size of the combustion product stream has a direct influence on the radiative heat flux.
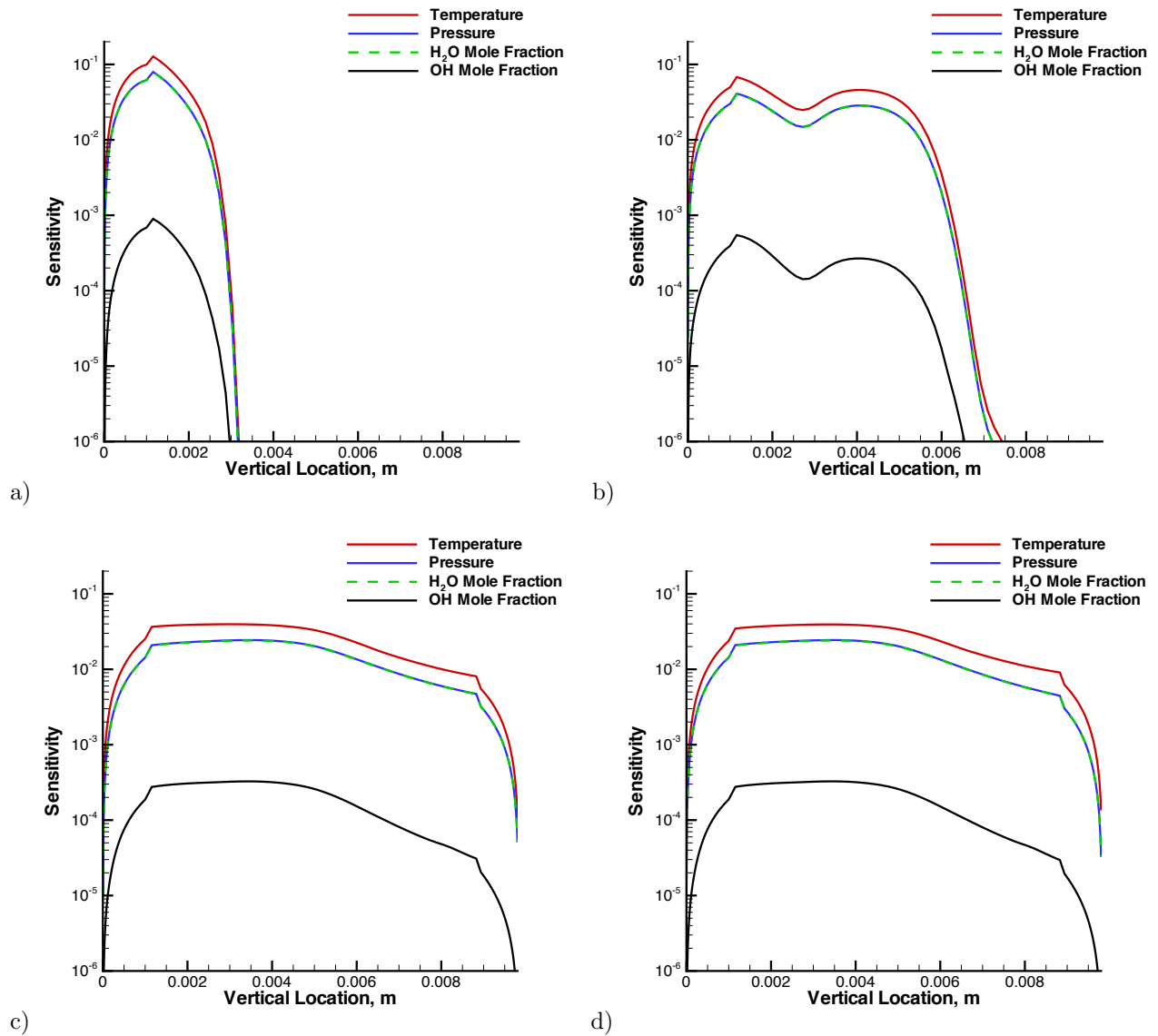
American Institute of Aeronautics and Astronautics

Figure 10. Radiative flux sensitivity ($\frac{\delta F}{\delta u}(z)/\frac{F}{u(z)}$) for y=0.006 m at (a) x=0.042 m lower wall, (b) x=0.092 m lower wall, (c) x=0.242 m lower wall, and (d) x=0.242 m upper wall

American Institute of Aeronautics and Astronautics

Table 4. Comparison of variations of data from Nelson and HyShot II test cases. The temperature, pressure and mole fraction quantities for the HyShot simulation are averages. The profiles used for the calculation are displayed in Fig. 6. The quantities for the Nelson cases are uniform throughout the flow domain.

Flow-field Data	Depth (cm)	Lower Wall Flux (W/m^2)	Temperature (K)	Pressure (Pa)	Mole Fraction H$_2$O	Mole Fraction OH
HyShot Exit	0.98	7.77×10^3	1967	2.190×10^5	0.137	0.0113
HyShot Exit	6.65	4.51×10^4	1967	2.190×10^5	0.137	0.0113
Nelson Mach 14	0.98	3.30×10^4	2924	4.752×10^5	0.205	0.0200
Nelson Mach 14	6.65	1.81×10^5	2924	4.752×10^5	0.205	0.0200
Nelson Mach 9.77	0.98	8.11×10^4	3091	8.886×10^5	0.269	0.0290
Nelson Mach 9.77	6.65	3.99×10^5	3091	8.886×10^5	0.269	0.0290
Nelson Mach 7.67(a)	0.98	3.59×10^4	2715	5.755×10^5	0.204	0.0200
Nelson Mach 7.67(a)	6.65	1.89×10^5	2715	5.755×10^5	0.204	0.0200
Nelson Mach 7.67(b)	0.98	6.18×10^3	1956	2.898×10^5	0.110	0.0150
Nelson Mach 7.67(b)	6.65	3.54×10^4	1956	2.898×10^5	0.110	0.0150

III.F.   Temperature change due to radiation

Another potential influence of radiative heat transfer on a flow is temperature reduction, which may change the flow characteristics and affect the combustion reaction rates. The per-volume heat loss due to radiation is depicted in Fig. 11(a), which is taken directly from the DOM flux solution. The change in temperature is derived by dividing the radiative heat loss in each cell by the density and specific heat. The rate of temperature reduction is high, but not significant. If a conservative calculation is made for the residence time of the radiating species based on an average velocity of 1000 m/s and a travel distance within the combustion chamber of 0.35 m, then the resulting residence time is 3.5×10^{-4}s. During this time, assuming that heat loss is constant, no part of the flow will lose more than 3K in temperature from radiation before exiting, as can be seen from Fig. 11(b). This means that interaction between different parts of the flow and losses per unit volume from radiation will both be small, even with conservative estimates of velocity and distance. These simulations are performed for cold nonreflective walls as well as for 2000K blackbody walls. The flow absorbs a significant amount of radiation from the radiative walls. This greatly reduces the magnitude of temperature reduction due to radiation. In certain locations, it causes a temperature increase. All of these changes are of smaller magnitude than the nonradiatve wall case. As such, radiative walls serve to maintain the flow temperature.
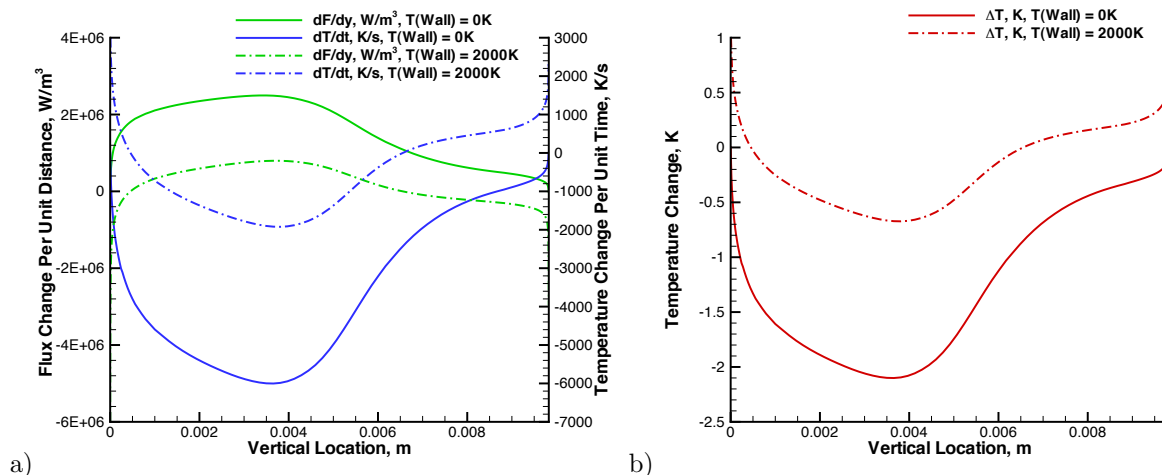

Figure 11.   Heat loss for a profile at x=0.242 m downstream from the vehicle tip with 0 K and 2000 K walls. (a) Volumetric heat loss vs. vertical position and temperature change per unit time vs. vertical position. (b) Estimated change in temperature vs vertical position

American Institute of Aeronautics and Astronautics

IV.   Conclusion

The radiative heat flux for the hydrogen fueled HyShot II scramjet combustion chamber was simulated using a one-dimensional DOM and a three-dimensional ray tracing radiation code. The simulations were based on CFD data computed by a chemically reacting k-ω RANS solver. The radiative heat flux and optical depths were shown to increase stream-wise through the engine as the hot combustion products were produced. The effects decreased as the flow expanded and cooled throughout the exit nozzle. The overall radiative heat flux to the combustion chamber walls was negligible compared to the convective heat flux. While this differed from previous works on supersonic combustion, the small chamber size, and the less aggressively radiating flow-fields present in the HyShot II combustor explained the differences. Overall, with its high speed and small geometry, the HyShot II combustion chamber was not greatly affected by radiative effects as shown by these preliminary analyses. As such, a more rigorous three-dimensional analysis is not justified. With this in mind, radiation may play a larger role in future scramjet tests if a larger geometry, more radiative fuel mixture, or physical flame holder is employed. Therefore, radiation should still be considered when different designs and test configurations are considered.

Future work will include expanding this analysis to larger scramjet engines with more radiative species such as HiFire 2.[23] Higher order DOM with a Statistical Narrow Band Correlated-k method can be added to provide better spatial and spectral resolution.[24] Finally, the adjoint sensitivity can be used to assist in uncertainty quantification methods as applied to phenomena inside a scramjet.[25]

Acknowledgments

References

[1]Boyce, R. R., Gerard, S., and Paull, A., "The Hyshot Scramjet Flight Experiment- Flight Data and CFD Calculations Compared," No. 2003-7029, AIAA, 2003.

[2]Karl, S., Hannemann, K., Mack, A., and Steelant, J., "CFD Analysis of the HyShot II Scramjet Experiment in the HEG Shock Tunnel," No. 2008-2548, AIAA, January 2008.

[3]Terrapon, V., Ham, F., Pecnik, R., and Pitsch, H., "A flamelet-based model for supersonic combustion," Annual research brief, Center for Turbulence Research, Stanford University, Stanford University, Stanford, CA 94305, 2009.

[4]Pecnik, R., Terrapon, V., Ham, F., and Iaccarino, G., "Full System Scramjet Simulation," Annual research brief, Center for Turbulence Research, Stanford University, Stanford University, Stanford, CA 94305, 2009.

[5]Nelson, H. F., "Radiative Heating in Scramjet Combustors," *Journal of Thermophysics and Heat Transfer*, Vol. 11, No. 1, 1997, pp. 59–64.

[6]Liu, J. and Tiwari, S. N., "Radiative Heat Transfer Effects in Chemically Reacting Nozzle Flow," *Journal of Thermophysics and Heat Transfers*, Vol. 10, No. 3, 1996, pp. 436–444.

[7]Tiwari, S. N., Pidugu, S. B., and Mohieldin, T. O., "Radiative Interaction in Supersonic Flows of Premixed Hydrogen in Expanding Nozzles," No. 99-1052, AIAA, January 1999.

[8]Gonçalves, R., Lecanu, M., Ducruix, S., Gicquel, O., Iacona, E., and Veynante, D., "Coupled Large Eddy Simulations of Turbulent Combustion and Radiative Heat Transfer," *Combustion and Flame*, Vol. 152, 2008, pp. 387–400.

[9]Pope, S. B., *Turbulent Flows*, Cambridge University Press, New York, 2000.

[10]Chandrasekhar, S., *Radiative Transfer*, Dover Publications Inc, New York, 1960.

[11]Goody, R. M. and Yung, Y., *Atmospheric Radiation Theoretical Basis*, Oxford University Press, New York, 2nd ed., 1989.

[12]Modest, M. F., *Radiative Heat Transfer*, Academic Press, San Diego, 2nd ed., 2003.

[13]Liu, L.-H., Tan, H.-P., and He, Z.-H., "Inverse Radiation Problem of Source Term in Three-Dimensional Complicatd Geometric Semitransparent Media," *International Journal of Thermal Sciences*, Vol. 40, 2001, pp. 528–538.

[14]Salinas, C. T., "Inverse Radiation Analysis in Two-Dimensional Gray Media using Discrete Ordiantes Method with a Multidimensional Scheme," *International Journal of Thermal Sciences*, Vol. 49, 2010, pp. 302–310.

[15]Coelho, P. J., Perez, P., and Hafi, M. E., "Benchmark Numerical Solutions For Radiative Heat Transfer in Two-Dimensional Axisymmetric Encolsures With Nongray Sooting Media," *Numerical Heat Transfer, Part B*, Vol. 43, 2003, pp. 425–444.

[16]Liou, K. N., *An Introduction to Atmospheric Radiation*, Academic Press, San Diego, 2nd ed., 2002.

[17]Fiveland, W. A., "Discrete Ordinate Methods for Radiative Heat Transfer in Isotropically and Anisotropically Scattering Media," *Journal of Heat Transfer*, Vol. 109, August 1987, pp. 809–812.

[18]Hirsch, C., *Numerical Computation of Internal & External Flows*, Butterworth-Heinermann, Oxford, UK, 2nd ed., 2007.

[19]Rao, S. S., *Applied Numerical Methods for Engineers and Scientists*, Prentice Hall, Upper Saddle River, NJ, 1st ed., 2002.

[20]Ludwig, C. B., Malkmus, W., Reardon, J. E., and Thomson, J. A. L., "Handbook of Infrared Radiation From Combustion Gases," Tech. Rep. SP-3080, NASA, 1973.

[21]Fidkowski, K. J. and Darmofal, D. L., "Output-Based Error Estimation and Mesh Adaptation in Computational Fluid Dynamics: Overview and Recent Results," No. 2009-1303, AIAA, January 2009.

[22]Smart, M. K., Hass, N. E., and Paull, A., "Flight Data Analysis of the Hyshot 2 Scramjet Flight Experiment," *AIAA Journal*, Vol. 44, No. 10, October 2006, pp. 2366–2375.

[23]Gruber, M., Smith, S., and Mathur, T., "Experimental Characterization of Hydrocarbon-Fueled, Axisymmetric, Scramjet Combustor Flowpaths," AIAA, April 2011.

[24]Joseph, D., Hafi, M. E., Fournier, R., and Cuenot, B., "Comparison of three spatial differencing schemes in discrete ordinates methods using three-dimensional unstructured meshes," *International Journal of Thermal Sciences*, Vol. 44, April 2005, pp. 851–864.

[25]Wang, Q., Duraisamy, K., Alonso, J. J., and Iaccarino, G., "Risk Assessment of Scramjet Unstart Using Adjoint-Based Sampling Methods," No. 2010-2921, AIAA, April 2010.